Biomedicine & Pharmacotherapy 171 (2024) 116017

Contents lists available at ScienceDirect

Biomedicine & Pharmacotherapy

journal homepage: www.elsevier.com/locate/biopha

Copper nitroprusside: An innovative approach for targeted cancer therapy via ROS modulation

Kanwal Asif [a,b], Muhammad Adeel [a,b,*], Md. Mahbubur Rahman [c], Michele Bartoletti [d,e], Simona Kranjc Brezar [f], Maja Cemazar [f], Vincenzo Canzonieri [a,g], Flavio Rizzolio [a,b,*], Isabella Caligiuri [a]

[a] Pathology Unit, Centro di Riferimento Oncologico di Aviano (C.R.O.) IRCCS, 33081 Aviano, Italy
[b] Department of Molecular Sciences and Nanosystems, Ca' Foscari University of Venice, 30172 Venice, Italy
[c] Department of Applied Chemistry, Konkuk University, Chungju 27478, South Korea
[d] Department of Medicine (DAME), University of Udine, Udine, Italy
[e] Unit of Medical Oncology and Cancer Prevention, Department of Medical Oncology, Centro di Riferimento Oncologico di Aviano (CRO), IRCCS, 33081 Aviano (PN), Italy
[f] Department of Experimental Oncology, Institute of Oncology Ljubljana, Zaloska cesta 2, SI-1000 Ljubljana, Slovenia
[g] Department of Medical, Surgical and Health Sciences, University of Trieste, 34149 Trieste, Italy

ARTICLE INFO

Keywords:
Self-therapeutic
Copper nitroprusside
Peroxynitrite
Self-supplying hydrogen peroxide

ABSTRACT

The clinical application of nanomaterials for chemodynamic therapy (CDT), which generate multiple reactive oxygen species (ROS), presents significant challenges. These challenges arise due to insufficient levels of endogenous hydrogen peroxide and catalytic ions necessary to initiate Fenton reactions. As a result, sophisticated additional delivery systems are required. In this study, a novel bimetallic copper (II) pentacyanonitrosylferrate (Cu(II)NP, Cu[Fe(CN) 5 NO]) material was developed to address these limitations. This material functions as a multiple ROS generator at tumoral sites by self-inducing hydrogen peroxide and producing peroxynitrite ($ONOO^-$) species. The research findings demonstrate that this material exhibits low toxicity towards normal liver organoids, yet shows potent antitumoral effects on High Grade Serous Ovarian Cancer (HGSOC) organoid patients, regardless of platinum resistance. Significantly, this research introduces a promising therapeutic opportunity by proposing a single system capable of replacing the need for H_2O_2, additional catalysts, and NO-based delivery systems. This innovative system exhibits remarkable multiple therapeutic mechanisms, paving the way for potential advancements in clinical treatments.

1. Introduction

ChemoDynamic therapy (CDT) is one of the promising therapeutic strategies in cancer therapy that utilize Fenton like chemistry to kill cancer cells, specifically [1–5]. In this system, the endogenous H_2O_2 reacts with the metal catalyst and produces reactive oxygen species (ROS) e.g., highly cytotoxic hydroxyl radicals ($^{\bullet}OH$) at the tumoral sites, which induce apoptosis [1,6,7]. This process is majorly depending upon two main factors: the amount of endogenous H_2O_2 at tumoral sites and the reactivity of the catalyst [2,8]. Although H_2O_2 in many cancer cells are higher than normal cells, unfortunately it is still insufficient to disassemble the nanomaterial into catalytic ions to achieve satisfactory CDT [1,9–11].

Several efforts have been devoted in the recent years to enhance endogenous H_2O_2 level at tumoral sites to amplify the oxidative stress by elevating the levels of $^{\bullet}OH$ generation [6,12,13], mainly following two approaches. Either it derives from the exogenous generation of H_2O_2, or from the endogenous production from the mitochondria. However, endogenous H_2O_2 in mitochondria decompose rapidly by cellular scavenging enzymes (catalases and peroxidases) before approaching the catalyst to initiate Fenton like reaction [2]. Hence, very low amount of $^{\bullet}OH$ are produced due to the low availability of endogenous H_2O_2. Many strategies have been taken to improve the exogenous H_2O_2 production near Fenton catalyst [12] but these systems are also oxygen dependent (to convert glucose into H_2O_2 and gluconic acid) [11,14] and need external stimuli, in turn limiting their therapeutic efficacy. An

* Corresponding authors at: Pathology Unit, Centro di Riferimento Oncologico di Aviano (C.R.O.) IRCCS, 33081 Aviano, Italy.
E-mail addresses: muhammad.adeel@unive.it (M. Adeel), flavio.rizzolio@unive.it (F. Rizzolio).

https://doi.org/10.1016/j.biopha.2023.116017
Received 9 August 2023; Received in revised form 7 December 2023; Accepted 14 December 2023
Available online 8 January 2024

alternative way to increase the H_2O_2 level in cancer cells is through metal peroxides (MPs) as H_2O_2 self-supplying agents [2,15]. MPs contain metal ions and the peroxo part that are used as self-supplying source of H_2O_2 production. Therefore, Fenton metal peroxides could act as H_2O_2 enhancers and have the ability to initiate Fenton like reactions [1,2].

Although these systems work well to achieve an acceptable therapeutic efficacy, an alternative system that have dual metals (ions) to initiate Fenton reaction at specific pH with the ability to generate cytotoxic radicals like peroxynitrite ($ONOO^-$) as apoptotic inducer it is desirable [16].

$ONOO^-$ is an endogenous reactive nitrogen species (RNS), produced after the reaction between nitric oxide (NO) and superoxide anion ($O_2^{\bullet-}$) [16–18]. Usually, the level of $O_2^{\bullet-}$ is higher in tumoral cells resulting in a preferential generation of $ONOO^-$ in the tumor microenvironment [16,17]. In comparison to other free radicals like NO and $^{\bullet}OH$, $ONOO^-$ is more toxic in damaging DNA, proteins, and lipids of the cancerous cells [18–20]. It also helps to destroy the dense extra cellular matrices (ECM) in solid tumors that often hinder the deep penetration of antitumor drugs, which can cause the poor performance of anticancer drugs [17].

Although, several studies are available that used NO delivery systems with other therapeutic systems e.g., chemotherapy or photodynamic therapy to generate $ONOO^-$ radicals [17,20], these approaches have still many limitations [21,22]. Recently, our group demonstrated such alternative system based on Fe^{2+} and Ag^+ metal to improve the CDT efficacy without the need of any external stimuli [23,24]. However, there are no materials available that could generate $ONOO^-$ radicals specifically at tumoral sites and at the same time used as self-supplying H_2O_2 CDT agent having dual Fenton initiator metals (Cu and Fe) without the requirements of any delivery system or the need of external stimuli to specifically kill cancer cells.

Herein, we propose a versatile nanoplatform with multiple functionalities bimetallic copper (II) pentacyanonitrosylferrate or copper (II) nitroprusside (Cu(II)NP) nanostructures with dual Fenton type metals that simultaneously act as self-supplying H_2O_2 as well as $ONOO^-$ nanogenerator at tumoral sites. Cu(II)NP disassembled at tumoral sites resulting in the formation of copper peroxides to enhance H_2O_2 levels and initiate a Fenton type reaction through catalytic ions (Fe^{+2}, Cu^{+2}). In addition, naturally present NO component in the material structure is released at tumoral sites and produced $ONOO^-$ through reacting with superoxide anion ($O_2^{\bullet-}$). Furthermore, the presence of Cu+ cations triggers damage to the lysosomal membrane following the generation of reactive oxygen species (ROS), resulting in the release of proteases (cathepsins) and ultimately leading to cell death.

As a proof-of-concept, copper (I) nitroprusside was also synthesized and compared throughout the results. It is noted that copper (I) nitroprusside is less potent compared to copper (II) nitroprusside. In our results, it was found that CuNPs showing biocompatibility towards normal cells and normal liver organoids while producing very toxic effects on tumoral cells and patient derived tumor organoids (PDTO). Contrarily, copper (I) nitroprusside produce less H_2O_2 than copper (II) nitroprusside, which demonstrate its less potency. Overall, a novel multifunctional CuNP material was developed to produce multiple ROS species with dual catalyst ions in acidic environment to address the existence CDT challenges.

2. Materials and methods

2.1. Chemicals and reagents

Anhydrous methanol (99.8%), sodium nitroprusside dihydrate ($Na_2[Fe(CN)_5NO]\cdot 2\ H_2O$, SNP, ≥ 99%), copper (I) chloride (CuCl, ≥99%), and copper (II) chloride ($CuCl_2$, ≥99%) were purchased from (Sigma-Aldrich,St. Louis, MO, USA). A Millipore Milli-Q Biocell A10 water purifying system was employed to prepare ultrapure water. A2780, A2780cis, U-87 MG (Sigma-Aldrich, St. Louis, MO, USA), MDA-MB-231 (Cell Biolabs, CA, USA) SK-OV-3, MCF-7, MRC-5 (ATCC, Manassas, VA, USA) cell lines were grown accordingly to the manufacturers' instruction. LysoTracker Green DND-26, Hoechst 33342, and rhodamine B were purchased from (ThermoFisher Scientific, Waltham, MA, USA). CellTiter-Glo® from (Promega, Madison, WI, USA), PE-Annexin V Apoptosis Detection Kit from Becton-Dickinson Franklin Lakes, NJ, USA). ROS-Glo™ H_2O_2 luminescence assay from (Promega, Madison, USA), DAX-J2 PON Green Kit was purchased from (AAT Bioquest, Sunnyvale, CA, USA), FluorSave™ reagent (Cat. # 345789; Millipore: Burlington, MA, USA), VectaShield ® mounting medium with DAPI (Cat. # H-1200–10; Vector Laboratories, Newark, CA, USA). qPCR Primers from from (Integrated DNA Technologies, Bologna, Italy).

2.2. Instrumentation and measurements

The crystal structure of the as synthesized CuNP was analyzed using an X-ray diffractometer (XRD, Philips, X'pert, Netherland) with a Cu Kα radiation (λ = 1.5406 Å). The chemical functionalities of CuNP were investigated with a Fourier transform infrared (FTIR) spectrophotometer (MIDAC, M4000, Westfield, MA, USA). Raman spectra of the samples were measured using a Raman Spectrophotometer (Horiba Scientific, Xplora Plus, France) at an excitation wavelength of 532 nm. The chemical composition, oxidation states, and the nature of bonding were analyzed by X-ray photoelectron spectroscopy (XPS, Thermo Scientific™ K-Alpha, ThermoFisher Scientific, Waltham, MA, USA). Field-emission scanning electron microscope (FE-SEM, Carl Zeiss Sigma VP, Jena, Germany) and transmission electron microscope (TEM, JEM-2100, JEOL, Tokyo, Japan) were used to investigate the morphologies of the samples. The atomic percentage of the elements present in CuNP was measured by an energy-dispersive X-ray spectroscopy (EDS) analyzer (INCAx-sight7421, Oxford Instruments, UK) equipped with the FE-SEM instrument. The optical absorption spectra of the samples were collected using a UV-Visible spectrophotometer (UV–VIS–31 Scan, ONDA, Modena, Italy). To evaluate IC50 values, Tecan infinite M1000 Pro instrument (Tecan, Mannedorf, Switzerland) was used to read luminescence. AnnexinV was evaluated with BD FACSCantoII instrument (BD Biosciences, San Jose, CA, USA). Fluorescence images were captured with a Leica DM5500B fluorescence microscope with a X-Cite 120 PC Q lamp. The chemiluminescent signal was developed through a chemiluminescent gel imaging system (ChemiDoc™ Touch Imaging System, Bio-Rad, Hercules, CA, USA) and analysed with Image Lab Software (Bio-Rad).

2.3. Synthesis of CuNP

Cu(II)NP was synthesized by a simple solution process. Briefly, 0.2 M SNP (40 ml, in methanol) was mixed with 0.2 M of $CuCl_2$ (40 ml, in methanol) at room temperature (RT). As soon as these solutions were mixed, an oily viscous and green colour precipitate was formed. The mixed solution was sonicated further for 30 min using an ultra-bath sonicator. Then, the precipitate was allowed to settle down and complete the reaction at RT for two days. Finally, the precipitate of Cu(II)NP was collected by centrifuge method, washed with methanol, and dried overnight in a vacuum oven at 40 °C. The formation of Cu(II)NP can be described according to the following reaction and listed in Table S2.

$$Cu^{2+} + [Fe(CN)_5NO]^{2-} \rightarrow Cu[Fe(CN)_5NO]$$

A similar solution process was employed for the synthesis of Cu(I)NP. The details for the synthesis of Cu(I)NP are described in the supporting information.

2.4. Cell viability

To determine the effect of CuNP on different cell lines, cells were seeded in 96 multiwell plates at the concentration of 1×10^3 (cancer cells) or 8×10^3 (MRC-5) cells and then treated with various six

concentrations (0.001, 0.01, 0.1, 1, 10 and 100 μg) of copper nitroprusside (Cu(I)NP, Cu(II)NP), copper chloride (CuCl, $CuCl_2$), sodium nitroprusside (SNP) and cisplatin (CisPt). After 96 h cell viability was measured using the CellTiter-Glo® assay system according to the manufacturer's instructions (Promega, Madison, WI, USA) with a Tecan M1000 instrument (Tecan, Mannedorf, Switzerland). IC_{50} values were calculated from non-linear regression method using GraphPad prism software.

2.5. Intracellular localization

Investigation of intracellular uptake of CuNP was conducted by fluorescent probes. In brief, A2780 cells were seeded at a density of 2×10^5 cells/ml on transparent microplate containing a glass coverslip. To label CuNP, 30 μg/ml of rhodamine B was mixed with CuNP at room temperature under continuous rotation. Then cell lines were treated with 10 μg/ml of CuNP for different time points (6, 12 and 24 h). After PBS twice washing cells were incubated according to the manufacturer's instructions with 200 nM of Lysotracker™Green DND-26 (ThermoFisher scientific, Waltham, MA, USA) for lysosomes and 200 ng/ml Hoechst 33342 for nuclear staining, respectively. Later, cells were fixed with 4% paraformaldehyde for 20 min and the coverslip was mounted using Fluorsave mounting media (Merck Millipore, Burlington, MA, USA) for cellular imaging. Hoechst, LysoTracker Green DND-26 and Rhodamine B were detected under a fluorescence microscope with appropriate filters. Image was analyzed with ImageJ and JacoP plugins.

2.6. Flow cytometry analysis

A2780 cells were seeded at density 2×10^5 in 6 multi well plates. Then cells were treated with 10 μg/ml of CuNP (Cu(I)NP, Cu(II)NP), CuCl, $CuCl_2$, SNP (10 μg/ml) or CisPt (3 μg/ml: 10 μM) for different time points (6 and 24 h). After treatment, cells were digested, collected and labelled with PE-Annexin V Apoptosis Detection Kit from (Becton-Dickinson, Franklin Lakes, NJ, USA) for 15 mins in darkness. Subsequently, then analysed by BD Canto II flow cytometer and BD FACS DIVA software.

2.7. Cytochrome c and cathepsin B release assay

A2780 and SKOV3 cells were seeded at a density of 2×10^5 cells/ml on coverslip glass inserted in 6-well plates. Cells were treated with CuNP (Cu(I)NP, Cu(II)NP) (10 g/ml) or CisPt (3 μg/ml: 10 μM) for 6, 12 and 24 h. Then cells were fixed with 4% paraformaldehyde (20 min, RT), permeabilized with 0.3% Triton X- 100/PBS (15 min, RT) and blocked in 8% BSA/PBS (1 h, RT). Later, Cells were stained with mouse monoclonal anti-cytochrome c (6H2. B4 antibody, 1:100 dilution in 1% BSA/PBS, at 4 °C, overnight) antibody obtained respectively from (Cell Signaling Technology, Cat. # 12963; Danvers, MA, USA) and labelled with secondary antibody (1: 1000 dilution, Alexa Fluor® 488 dye, RT, 2 h) obtained from (Cell Signaling Technology Cat. # 4408; Danvers, MA, USA), or with rabbit polyclonal anti-Cathepsin B (FL-339) obtained respectively from (Santa Cruz Biotechnology, Cat. # 13985; Dallas, TX, USA) (1:100 dilution in 1% BSA/PBS, at 4 °C, overnight) and labelled with secondary antibody (Alexa Fluor® 555 dye, 1:1000 dilution, RT, 2 h) obtained from (Cell Signaling Technology Cat. # 4412 S; Danvers, MA, USA). To visualize DNA, cells were stained with DAPI 1 mg/ml (1:10000 dilution in PBS, RT, 1 min). Cells were washed three times with PBS after all incubations. All the coverslips were mounted in fluorSave™ reagent (Cat. # 345789; Millipore: Burlington, MA, USA). The cells were examined with a Leica DM5500B fluorescence microscope with a X-Cite 120 PC Q lamp and the images were analyzed with Image J software.

2.8. H_2O_2 level measurement

To measure H_2O_2 level A27890, SK-OV-3, MRC-5 were seeded in 96 multiwell plates 1×10^4 per well and were cultured at 37.0 °C for 24 h. Then cells were treated with 10 μg/ml of CuNP (Cu(I)NP, Cu(II)NP), CuCl, $CuCl_2$, SNP (10 μg/ml) or CisPt (3 μg/ml: 10 μM) for different time points (6, 12 and 24 h). After specific time points oxidative stress was measured using ROS-Glo™ H_2O_2 luminescence assay (Promega, Madison, WI, USA) according to manufacturer's instructions and then read with a Tecan M1000 instrument.

2.9. Intracellular peroxynitrite ($ONOO^-$) detection

A2780, SK-OV-3, MRC-5 were seeded in 96 multiwell plates at a density of 4×10^4 per well and were cultured at 37.0 °C for 24 h. The cells were treated with CuNP (Cu(I)NP, Cu(II)NP), CuCl, $CuCl_2$, SNP (10 μg/ml) or CisPt (3 μg/ml: 10 μM) for 24 h. After that, the cells were stained with DAX-J2 PON Green Cell Meter Fluorometric Peroxynitrite Assay Kit (AAT Bioquest, Sunnywale, CA, USA) at 37 °C for 2 h in the darkness. After $ONOO^-$ generation was measured quantitatively using microplate reader. The excitation and emission filter settings for the microplate reader were 490 nm and 530 nm, respectively.

2.10. qRT-PCR analysis

Total RNA was isolated from A2780 and SK-OV-3 cells after 24 h treatment of CuNP (Cu(I)NP, Cu(II)NP), CuCl, $CuCl_2$, SNP (10 μg/ml) or CisPt (3 μg/ml: 10 μM) using RNA extraction mini kit InviTrap® Spin Universal RNA Mini Kit from (AB ANALITICA, Padova, Italy) following quantification using spectrophotometer. cDNA was synthesized from total RNA (0.4 μg) using cDNA synthesis kit GoScript™ Reverse Transcriptase from (Promega, Madison, WI, USA). Followed transcribed by Promega qPCR Master mix kit (GoTaq® qPCR Master Mix, Promega). The primers used for qPCR is listed in Table S5 ordered from Integrated DNA Technologies (Bologna, Italy). Thermal cycling reaction conditions included an initial denaturation at 95℃ for 10 min, followed by 45 cycles of denaturation at 95℃ for 15 s and annealing at 60 °C performed by QuantStudio Applied Biosystem and relative gene expression (2ˆddCT) was normalized with β-actin housekeeping gene expression.

2.11. Organoid isolation and culture

Mouse liver organoids were created from 8-week-old C57/BL6 mice following the protocol described by Stappenbeck [34]. Organoids were created from mouse liver post-mortem (Italian Ministry of Health, 148/2016-PR). Briefly, piece of liver tissue was dissected and after 30' enzymatic digestion of 2 mg/ml collagenase followed centrifugation collected pellet resuspended in Cultrex growth factor-reduced Basement Membrane Extract (BME), Type2 (R&D Systems Cat. # 3533–001-02, Milan, Italy) and seeded in 24 multi well. After solidification of matix 450 μl of organoid medium was added.

Patient derived Tumour organoids (PDTO) were obtained from totally anonymized specimens. However, biobank informed consent for research purposes was available to collect the samples at National Cancer Institute (CRO) of Aviano. Tissues were handled and cultured using the protocol described for the isolation of mouse liver organoids.

2.12. Toxicity assay on mouse liver organoids

Toxicity test on mouse liver organoids was conducted by treating organoids (five replicates) on 96-MW with CuNP (Cu(I)NP, Cu(II)NP), CuCl, $CuCl_2$, SNP (10 μg/ml) ranging from 100 μg to 0.034 μg for 96 h. As positive control, we used CisPt starting from (30 μg/ml: 100 μM) to (0.009 μg/ml: 0.03 μM). The cytotoxicity was correlated with the cell viability evaluated by CellTiter-Glo® Luminescence assay (Promega, Madison, WI, US) with Tecan M1000 instrument (Tecan, Mannedorf, Switzerland).

2.13. Toxicity assay on patient derived tumour organoid (PDTO)

Cytotoxicity test on Patient Derived Tumour Organoid (PDTO) were conducted at passage zero. PDTO were plated on 96 Multi well and treated with (Cu(I)NP, Cu(II)NP) ranging from 100 μg to 0.034 μg for 96 h, CisPt ranging from (30 μg/ml: 100 μM) to (0.009 μg/ml: 0.03 μM) for 96 h. Cell viability was assessed by CellTiter-Glo®Luminescence assay (Promega, Madison, WI, US) with an Infinite200 PRO instrument (Tecan, Switzerland). IC_{50} values were analyzed from non-linear regression method using GraphPad prism software.

2.14. Histopathological analysis of HGSOC organoids

Formalin-fixed paraffin-embedded section of ascites and solid tumour organoids were used for histopathological analysis. Organoids were collected, fixed in phosphate-buffered 10% formalin, and embedded in paraffin using Micro NextGen Cell Blocking™ Kit (Cat n°: M20; AV Bioinnovation) following manufacture instructions. Following, 5 μm sections were stained with haematoxylin and eosin (H&E) by using the Leica ST5020 multistainer and 2 μm sections were cut for immunohistochemistry (IHC) analysis. Heat-induced antigen retrieval method and UltraVision LP Detection System HRP DAB kit (Thermo Scientific, Waltham, USA) was used to performed IHC staining. The following antibodies were used to characterize patient's derived Tumour Organoid

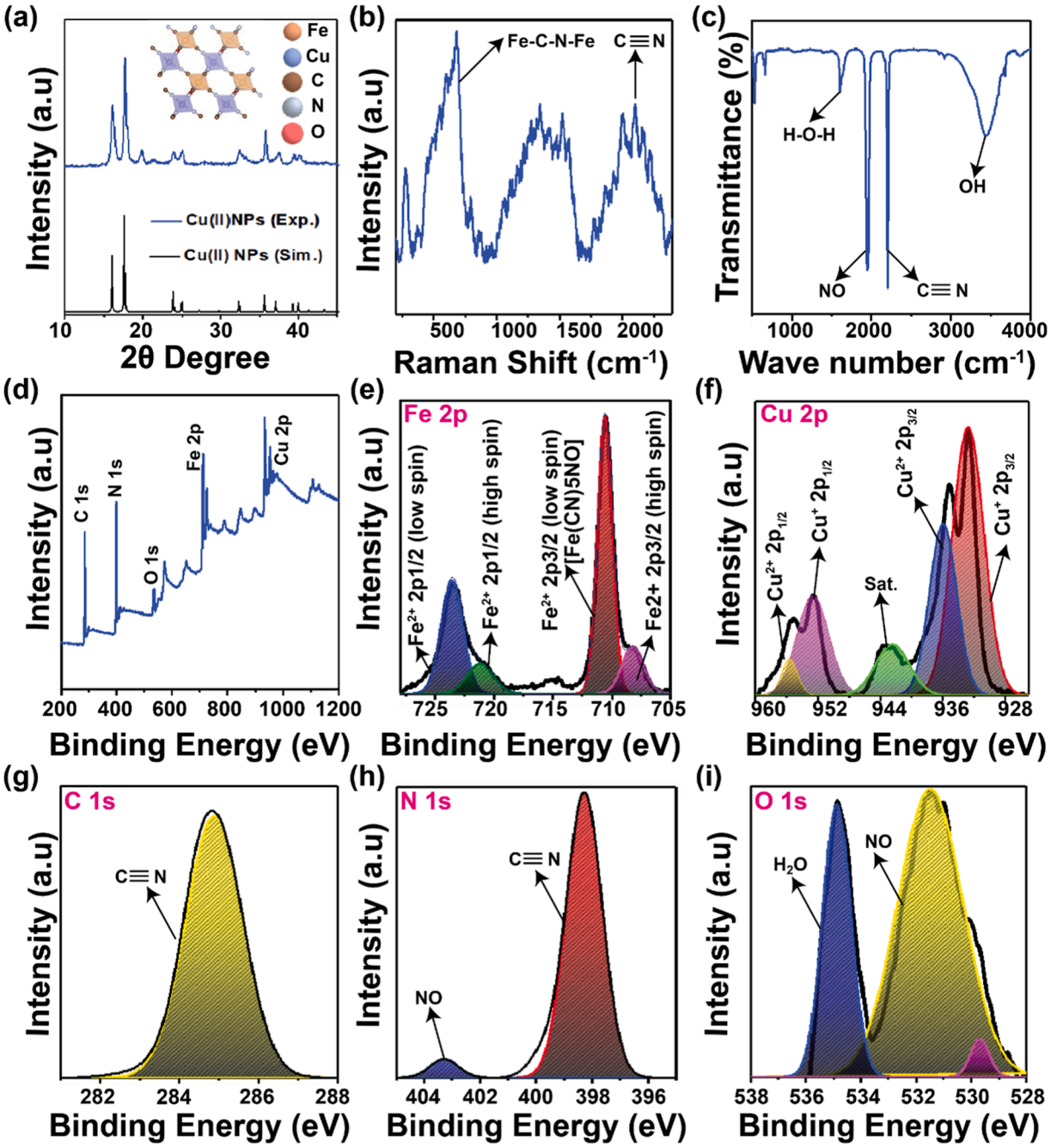

Fig. 1. Structural characterization of CuNP. a, Powder XRD pattern of as-synthesized Cu(II)NP together with the simulated XRD pattern (inset shows the crystal structure of Cu(II)NP). **b,** Raman and **c,** FTIR spectra of Cu (II)NP. **d,** XPS survey spectra of Cu (II)NP and high-resolution XPS spectra of **e,** Fe 2p, **f,** Cu 2p, **g,** C 1 s, **h,** N 1 s, and **I,** O 1 s in Cu(II)NP. The solid lines and the shaded region indicate the experimental and fitted data, respectively.

and parent tumour: PAX8 (Cat. # 10336–1-AP, ProteinTech Group, Germany, EU) Ca125 (Cat. # sc-52095, Santa Cruz Biotechnology, Dallas, USA) and WT1 (Cat. # ab89901, Abcam, UK). Tissues were analyzed with a light microscope using different magnifications.

2.15. Animal studies

Animal experiments (EU directive (2010/63/EU) were conducted under the authorization of the National Ethical Committee and the Administration of the Republic of Slovenia for Food Safety, Veterinary and Plant Protection.

The tumor-bearing mice were randomly allocated into 3 groups (n = 4 tumors per group). Mice per group were treated intraperitoneally (i.p.) with vehicle, 4 mg/kg of Cu(II)NP and 2 mg/kg of CisPt. Following treatments, mice were monitored every day for toxicity signs for 24 days. Data are reported as the mean and standard error.

2.16. Statistical analysis

Statistical analysis was performed with GraphPad Prism software and a p-value < 0.05 was considered significant.

3. Results and discussion

3.1. Structural information of CuNP

Fig. 1**a** shows the powder XRD pattern of Cu(II)NP together with the computed XRD pattern. The XRD pattern of the as-synthesized Cu(II)NP is well-matched with the simulated XRD pattern with sharp and intense peaks corresponding to the highly crystalline of Cu(II)NP. In detail, the major peaks at $2\theta = 16.0^{o}$, 17.63^{o}, 23.84^{o}, 25.05^{o}, 32.40^{o}, 35.77^{o}, and 37.47^{o} could be attributed to the *hkl* reflections of the (11−1), (1−10), (20−1), (1−1-1), (22−2), (2−20) and (22−1) planes, respectively, of the tetragonal crystal system belonging to the space group *I4mm*, as shown in the inset **(**Fig. 1**a)** [25]. The powder XRD pattern of Cu(I)NP presented the possible monoclinic (space group *Pc*) or triclinic (*P-1*) crystal structures, isostructural to the monovalent Ag^{+} and Hg^{+} based nitroprussides, respectively **(**Fig. S1a**)** [25,26]. For elucidating the exact crystal structure and the XRD pattern of Cu(I)NP, single-crystal preparation and the corresponding XRD analysis are required that is beyond the scope of this research. The high intensity and sharp XRD peaks of Cu (I)NP suggest the high crystallinity of the as-prepared sample. The composition and the crystal structures of Cu(II)NP and Cu(I)NP were analyzed further by Raman spectroscopy, as shown in Fig. 1**b** and Fig. S1b, respectively. Both Cu(II)NP and Cu(I)NP exhibited a high-intensity Raman peak at about 2106 cm^{-1}, which could be attributed to the stretching band of the C≡N group [27]. The other high-intensity Raman band for Cu(II)NP located at 275 and 680 cm^{-1} and for Cu(I)NP peaked at 280 and 670 cm^{-1} could be ascribed to the Fe–C–N–Fe bands in both the materials, while the peaks at 680 cm^{-1} for Cu(II)NP and 670 cm^{-1} for Cu(I)NP could be additionally assigned to the presence of Fe-NO band in the samples [27–29]. Fig. 1**c** and Fig. S1c show the FTIR spectra of the as-prepared Cu(II)NP and Cu(I)NP, respectively, representing the nature of the chemical species present in these materials. Both the materials showed a strong O−H absorption band of water at about 3441.97 cm^{-1} together with the deformational scissor vibrations band of water at 1609 cm^{-1} and 1628 cm^{-1}, respectively, for Cu(II)NP and Cu(I)NP [29]. These O−H bands were possibly originated from the adsorbed water molecules as well as crystalline water in the samples. The intense bands of NO and C≡N shown in both spectra at about 1955.43 cm^{-1} and 2217.06 cm^{-1} respectively, are in line with the reported results [29,30].

XPS spectra were measured for both materials to confirm the elements, functional groups, and elemental oxidation states. Fig. 1**d** and Fig. S1d display the survey XPS spectra Cu (II)NP and Cu(I)NP, respectively. The spectra showed the presence of C 1 s, N 1 s, O 1 s, Fe 2p, and Cu 2p peaks in their reported binding energy values [31]. Fig. 1 **(e-i)** presents the high-resolution XPS spectra of Fe 2p, Cu 2p, C 1 s, N 1 s, and O 1 s, respectively, in Cu(II)NP, and the binding energies of characteristic functional groups and elemental peaks are summarized in Table S1. The deconvoluted core-level spectra of Fe 2p displayed high-intensity spin-orbit doublets peaks of Fe $2p_{3/2}$ and Fe $2p_{1/2}$ with Fe^{2+} low spin state at 710.55 and 723.50 eV, respectively, originated from the Fe^{2+} species, $[Fe(CN)_5NO]$, in Cu(II)NP [29,32]. The other low-intensity peaks for Fe 2p at 708.16 and 721.17 eV could be assigned to the Fe $2p_{3/2}$ and Fe $2p_{1/2}$, respectively, with high-spin Fe^{2+}, created by the partial decomposition of Cu(II)NP during the XPS experiment. The appearance of a weak satellite peak at 714.50 eV further confirmed the presence of high spin Fe^{2+} [32]. This is possibly occurred by altering the C≡N bonds from Fe-CN to Fe-NC or breaking of F-CN bond induced by the high-energy electron beam during XPS measurements. The deconvoluted and the fitted Cu 2p spectra in Cu(II)NP exhibited the presence of reduced Cu^{+} species (Cu^{+} $2p_{3/2}$ = 932.76 eV and Cu^{+} $2p_{1/2}$ = 952.61 eV), in contrast with Cu^{2+} (Cu^{2+} $2p_{3/2}$ = 935.97 eV and Cu^{2+} $2p_{1/2}$ = 956.62 eV) in the original samples [29,32]. The appearance of these high-intensity Cu^{+} peaks could be ascribed to the decomposition of Cu(II)NP during XPS measurement, consistent with the XPS spectra of Fe 2p. Further, it can be concluded that the Cu^{+} species might be present in the degraded Cu(II)NP as CuCN by breaking the Fe-CN bond [32]. In contrast, the core-level Cu 2 P spectra of Cu(I)NP showed the presence of Cu^{2+} (Cu^{2+} $2p_{3/2}$ = 935.70 eV and Cu^{2+} $2p_{1/2}$ = 956.79 eV), in contrast with Cu^{+} species (Cu^{+} $2p_{3/2}$ = 932.74 eV and Cu^{+} $2p_{1/2}$ = 952.50 eV) in Cu(I)NP, as shown in Fig. S3a. However, the intensity ratio of Cu^{+} $2p_{3/2}$/Cu^{2+} $2p_{3/2}$ (2.66) in Cu(I)NP is much higher than the intensity ratio of Cu^{+} $2p_{3/2}$/Cu^{2+} $2p_{3/2}$ (1.55) in Cu(II)NP. This suggests the successful formation of Cu(I)NP, however, the presence of Cu^{2+} might be originated by the partial oxidation of Cu(I)NP induced by air or XPS electron beam. The high-resolution C 1 s spectrum of Cu(II)NP showed only C≡N peak at 284.82 eV without the presence of any impurity peak, while N 1 s spectra showed the C≡N and NO peaks at the binding energies of 398.30 and 402.27 eV, respectively, consistent with the reported results [29,32]. The fitted O 1 s spectra of Cu(II)NP comprised two-component peaks at 531.45 and 534.80 eV, which could be ascribed to the NO and oxygen peaks (arising from the crystalline or adsorbed water molecules) [29]. A similar Fe 2p, C 1 s, N 1 s, and O 1 s spectra were observed for Cu(I)NP respectively, consistent with its chemical formula **(**Fig. S3 **(b-e)**.

3.2. 2D high resolution structure of CuNP

Fig. S2 shows the FE-SEM images of Cu(II)NP with different magnifications and the corresponding HR-TEM images are presented in Fig. S4. The images clearly demonstrated the formation of 2D nanosheets morphology of Cu(II)NP with the thickness of 30–50 nm and without the presence of aggregated nanosheets. This is further evidenced by the high transparency of nanosheets to the electron beam, as observed in the HR-TEM images. In contrast, Cu(I)NP displayed 1D nanorod morphologies with a diameter from 100–120 nm, as shown in the FE-SEM **(**Fig. S5 **(a-b))** and HR-TEM **(**Fig. S5 **(c-d)** images. The EDS spectra of both Cu(II)NP **(**Fig. S2c**)** and Cu(I)NP **(**Fig. S5e**)** displayed the high-intensity peaks of Fe, Cu, O, C, and N without the presence of other elemental peaks, consistent with their corresponding chemical structures.

3.3. CuNP induce apoptotic cell death

The efficacy of the proposed CuNP was demonstrated mostly on ovarian cancer cell lines (A2780, A2780 cis, SK-OV-3) and in other tumoral cell lines including MDA-MB-231, MCF-7 breast cancer and U-87 MG glioblastoma cell lines to show the promising efficacy and comparable results among different cancer types **(**Fig. 2 **(a-f))**.

The IC_{50} values of CuNP against cancer cell lines are in the range

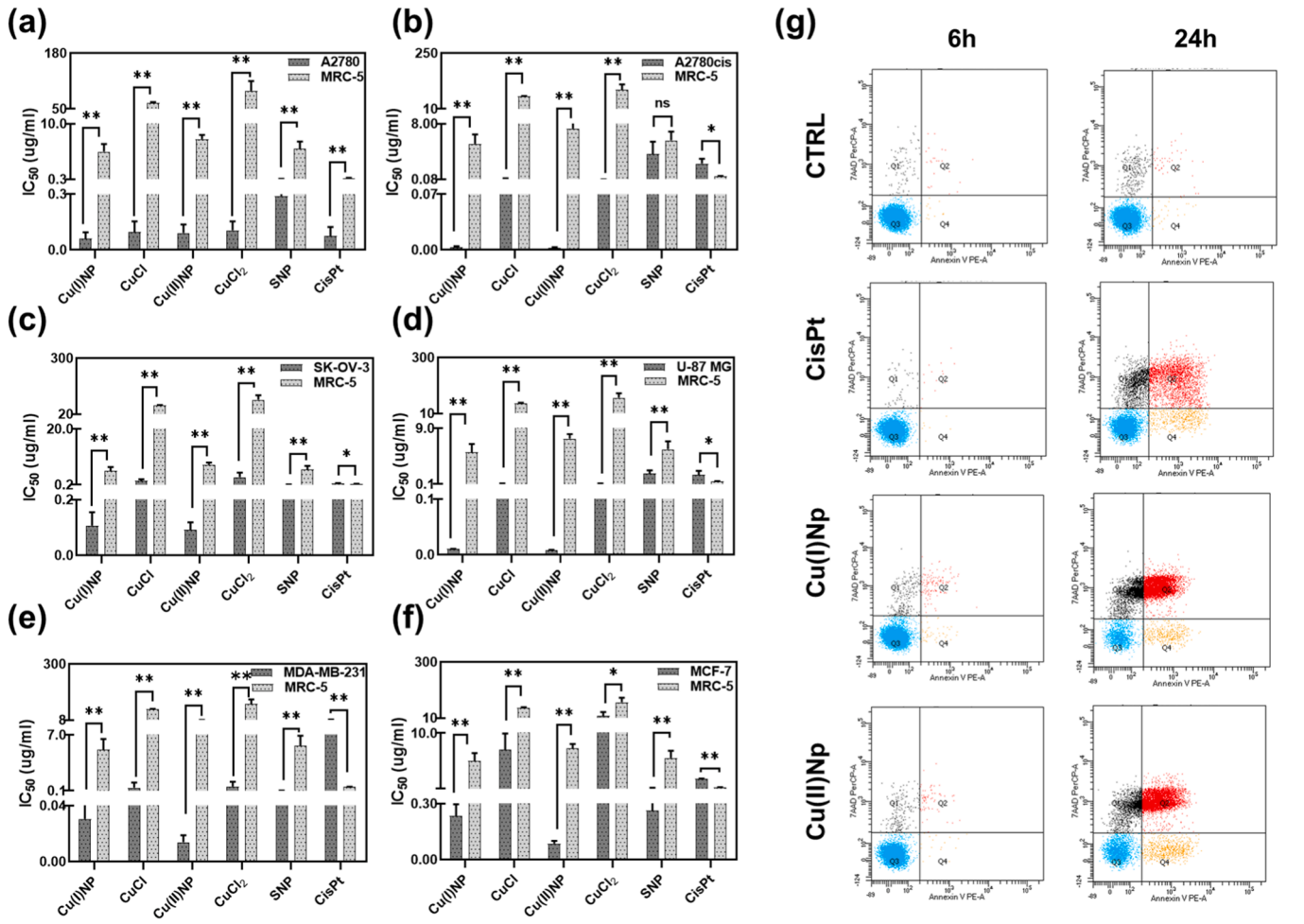

Fig. 2. Effects of CuNP on cell viability. **a-f,** IC-50 values of CuNP toward normal and cancer cells. Values are expressed as μg/ml. **g,** Apoptosis analysis. The A2780 cell line was analyzed by FACS using Annexin V/7AAD double staining after 6 and 24 h of CuNP (10 μg/ml) and CisPt (3 μg/ml; 10 μM) treatments. (Q3: Viable cells, Q4: Early apoptosis, Q2: Late apoptosis, Q1: Necrosis). Groups were considered statistically significant if $p < 0.05$ (*), $p < 0.01$ (**) or non-significant (ns); number of samples ($n = 3$).

between 0.002–0.2 μg/ml in comparison to the precursors (CuCl and $CuCl_2$ 0.08–32 μg/ml) as depicted in Fig. 2 **(a-f)**. Compared to CisPt on cancer cells, CuNP is more potent up to 1165-fold. On the other hand, in MRC-5 (normal human fibroblasts) the toxicity of CuNP is about ten times less than CisPt. This data demonstrated that inside the cells, CuNP could release Cu^{+} ions, which produce ROS species and exert their specific toxicity on cancer cells more than normal cells.

The full IC_{50} values are presented in Table S3. Taken together, these data suggest that Cu(I)NP and Cu(II)NP both have similar in vitro toxicity and induce significant toxicity in all cancer cell lines while having negligible effect on normal cells. Even, CuNP are very active on A2780cis cell line, overcoming the drug resistance mechanism related to cisPt. Additionally, a lower concentration of CuNP is required to induce cytotoxicity in comparison to most Fenton-like nanocatalysts reported till now, which require higher doses and exogenous additives to attain the desired cytotoxicity [33–37].

To understand the mechanism of action, annexin V/7AAD apoptosis assay was performed. A2780 cell line was incubated with CuNP (Cu(I) NP, Cu(II)NP), (CuCl and $CuCl_2$) (10 μg/ml) and cisPt (3 μg/ml; 10 μM) as a reference drug for 6 and 24 h. FACS analysis showed that the apoptosis increases over time. As shown in Fig. 2**g**, Cu(I)NP and Cu(II) NP induce a similar percentage of apoptotic cells: 0.3% vs 0.1% early and 0.9% vs 0.4% late apoptosis after 6 h of treatments, respectively. While 3.6% vs 5.8% early and 47% vs 42% late apoptosis after 24 h, respectively, which are significantly higher than control and CisPt group presented in Fig. 2**g**. Comparatively, the apoptosis ratio in precursor groups is much lower than CuNP treated group (Fig. S6**)**. The results demonstrated that CuNP efficiently kill the cancer cells mainly through apoptosis.

The cytochrome *c* release from mitochondria to cytoplasm is considered a major event during early stage of apoptosis [38]. Therefore, a cytochrome *c* release assay was done to evaluate the cell death at different time points. A2780 and SK-OV-3 were incubated with Cu(I)NP, Cu(II)NP (10 μg/ml) and CisPt (3 μg/ml; 10 μM) for 6, 12 and 24 h. As shown in Fig. 3 **(a,b)** green fluorescence demonstrated the release of cytochrome *c* after 6 h of CuNP treatment in a time dependent manner in both A2780 and SK-OV-3 cell lines. While cisPt consistently releases the cytochrome *c* after 12 h in both A2780 and SK-OV-3 cell lines which demonstrating the potency of CuNP in comparison to CisPt.

3.4. *Intracellular Localization of CuNP*

Intracellular distribution of CuNP was performed on A2780 and SK-OV-3 cell lines to evaluate the amount of CuNP transport to lysosomes. Cells were treated for 6, 12 and 24 h with Cu(I)NP and Cu(II)NP (10 μg/ml) and CisPt (3 μg/ml; 10 μM) followed by the labelling of the nucleus with Hoechst 33342 (blue), lysosomes with Lysotracker™Green DND-26 (green) and CuNP with rhodamine B (red). As illustrated in Fig. 4 **(a, b)** CuNP were predominantly co-localized with lysotracker in the cells, as determined by the strong yellow colour. The colocalization of CuNP and

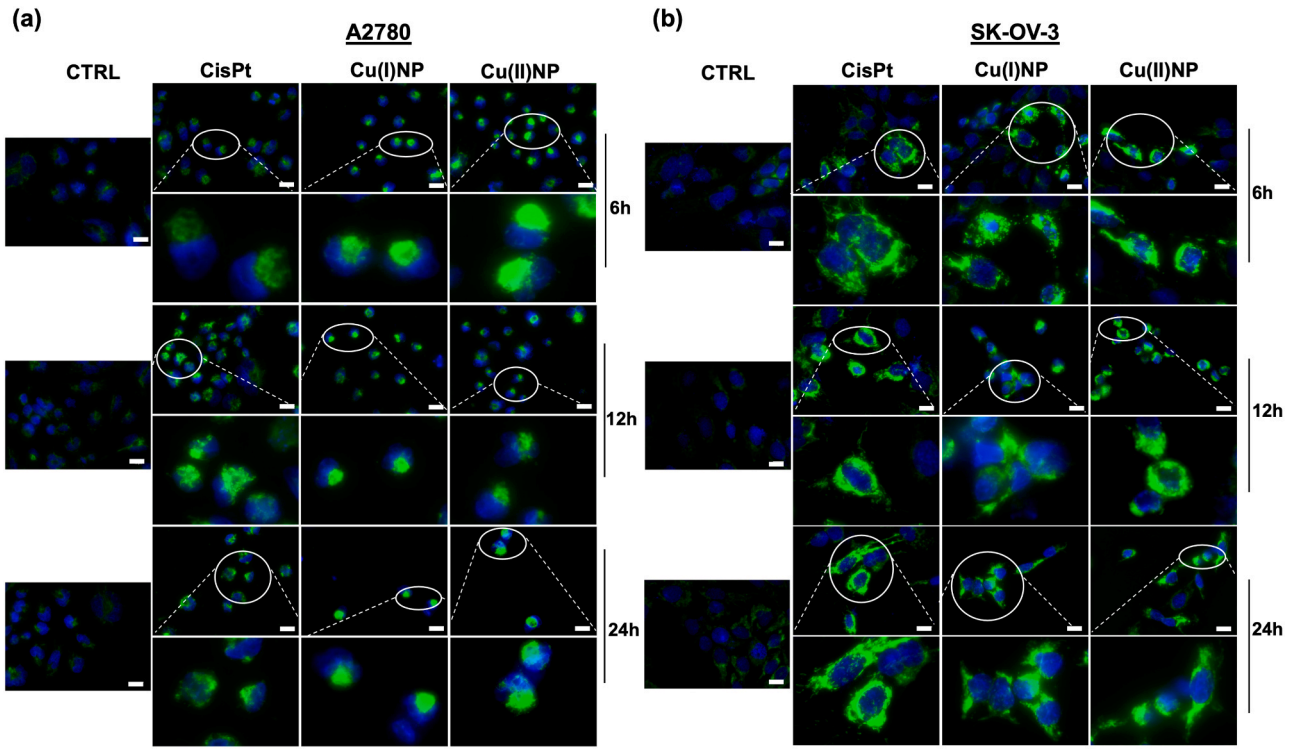

Fig. 3. Immunofluorescence analysis of cytochrome *c* release. a, A2780, **b,** SK-OV-3 treated with CuNP (Cu(I)NP, Cu(II)NP) (10 μg/ml) and CisPt (3 μg/ml; 10 μM) for 6, 12 and 24 h. Scale bar: 10 μm.

lysosomes was evaluated with Pearson's correlation coefficient (R) after 24 h. It was observed that NP completely localize in lysosomes at earlier timepoint but after 24 h, CuNP escape lysosomes. The "R" values after 24 h were 0.70 and 0.56 in A2780 and 0.554 and 0.448 in SK-OV-3 cell lines for Cu(I)NP and Cu(II)NP, respectively (Fig. 4 **(a,b)**. A time dependent decrease in lysotracker signal due to lysosomal membrane permeabilization was observed. Published data demonstrated that Cu^{+} cations induced lysosomal membrane damaged through ROS production contributing to the leak of proteases (cathepsins) and resulting in cell death [39,40]. Lysosomal membrane damaged is followed by the translocation of cathepsins from the lysosomes to the cytosol leading to the apoptosis [41–43]. To investigate cathepsin release, A2780 and SK-OV-3 cells were treated with Cu(I)NP, Cu(II)NP (10 μg/ml), CisPt (6 μg /ml) for 6, 12 and 24 h. After treatment, cathepsin B fluorescent staining was detected in a diffuse pattern, which increased over time (Fig. 4 **(c,d)** due to lysosomal membrane permeabilization (LMP). These results revealed that CuNP degrade the lysosomes due to the ROS production, which leads to LMP followed by cell death. To confirm that the cell death was due to oxidative stress, the intracellular ROS production was evaluated.

3.5. CuNP induces multiple ROS generation

To confirm that cell death was due to oxidative stress, A2780, SK-OV-3 cell lines and MRC-5 were incubated with CuNP, CuCl and $CuCl_2$ (10 μg/ml) and CisPt (3 μg /ml) for 6, 12 and 24 h. As displayed in Fig. 5 **(a-c),** over time there is a significant surge in H_2O_2 levels compared to the control and fibroblasts. In A2780, Cu(I)NP caused ~16 fold increase while Cu(II)NP caused ~31 fold increase in H_2O_2 levels after 24 h (Fig. 5**a)**. In SK-OV-3, Cu(I)NP caused ~9.2 fold increase and Cu(II)NP ~17 fold increase in H_2O_2 levels after 24 h (Fig. 5**b)**. However, in MRC-5 there is a little change after CuNP exposure in H_2O_2 level; Cu(I)NP caused ~1.6 fold increase while Cu(II)NP caused ~3.4 fold increase in ROS levels compared to control (Fig. 5**c)**. Whereas the precursors (CuCl and $CuCl_2$, SNP) caused more ROS production in normal cells in comparison to CuNP treated groups (Fig. S7 **(a-c))**. These results suggested that CuNP and specifically Cu(II)NP produced more ROS in tumor cells compared to fibroblasts since tumor cells are more sensitive for Fenton like reaction of Cu due to acidic environment. Additionally, NO delivery could enhance specific effect through peroxynitrite generation, which induced apoptosis after the interaction of NO with superoxide anion, which usually are produced from cancer cells [16].

$ONOO^{-}$ is another highly reactive species, which is generally generated from the reaction between ROS (mainly $O_2^{\bullet-}$) and NO [44]. $ONOO^{-}$ is known as an apoptotic inducer of damage to a number of molecules including DNA and proteins, leading to cell death. Therefore, to investigate ONOO− , DAX-J2 PON Green probe was used and quantitatively measured. As shown in Fig. 5 **(d,e)** after 24 h of treatment, there is a significant induction of fluorescence intensity in CuNP treated cells compared to control and fibroblasts. In A2780, Cu(I)NP caused ~1.3 fold increase while Cu(II)NP caused ~1.2 fold increase in $ONOO^{-}$ levels (Fig. 5**d)**. In SK-OV-3, Cu(I)NP caused ~2.3 fold increase and Cu (II)NP ~1.8 fold increase in $ONOO^{-}$ levels after 24 h (Fig. 5**e)**. However, in MRC-5 cells there is a slight change after NP exposure in $ONOO^{-}$ level; Cu(I)NP and Cu(II)NP caused ~0.9 fold decrease in $ONOO^{-}$ levels compared to control (Fig. 5 **(d,e))**. Whereas $ONOO^{-}$ levels in cancer cells treated with CuCl, $CuCl_2$ and SNP are slightly increased (Fig. S7 **(d, e))**. These results suggested that CuNP also produced more $ONOO^{-}$ in tumor cells compared to fibroblasts because generally there are more oxide species, which react with NO to produce the peroxynitrite specie [16].

3.6. CuNP induces oxidative stress

qPCR analysis was conducted to unravel the specific molecular events involved in the oxidative stress after 24 h of CuNP treatment in both cell lines, A2780 and SK-OV-3. The expression of antioxidant genes NRF2, HO-1 and SOD1 was evaluated. As previously reported, NO donors inhibited c-myc expression by inactivating Nf-κB [45,46] and reduced iNOS expression as a negative feedback [47].

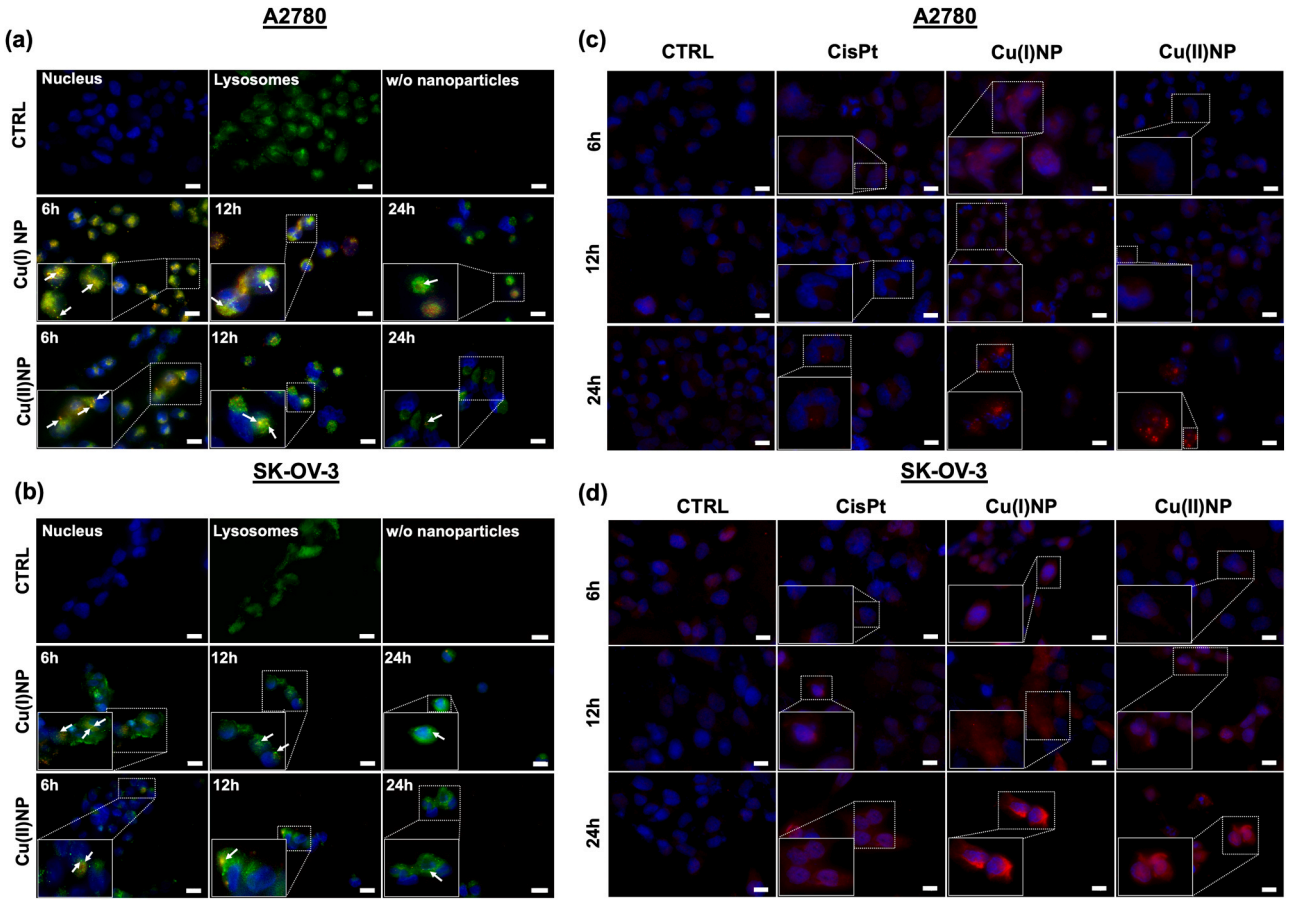

Fig. 4. Lysotracker analysis of CuNP for lysosomal internalization study. Fluorescence microscopy images of rhodamine-labeled CuNP. **a,** A2780, **b,** S-KO-V3 ovarian cancer cell lines after 6, 12 and 24 h. Controls (nuclei, lysosomes and only Rodamine w/o nanoparticles) were used to set-up fluorescence intensity and avoid background signals. Arrows indicate the colocalization of nanoparticles with lysosomes (yellow). **c,** A2780, **d,** SK-OV-3 immunofluorescence images of Cathepsin B release (red) after 6, 12 and 24 h of treatment of CuNP (Cu(I)NP, Cu(II)NP) (10 μg/ml) and CisPt (3 μg/ml; 10 μM) for 6, 12 and 24 h. Scale bar: 10 μm.

Under normal condition, NRF2 binds with Keap1 gene, which inhibits its activation followed by degradation, while when ROS are produced inside cells, NRF2 is released from Keap1 and translocated into the nucleus where it activates others antioxidant response genes including HO-1 [48,49]. In our results, we found that HO-1 expression is significantly upregulated in both cell lines after CuNP treatment compared to control. Our findings parallel with other results, which demonstrated that HO-1 expression is regulated by NRF2 in response to oxidative stress after copper nanoparticles treatment [50] (Fig. 5 **(f,h)**).

Cu/Zn superoxide dismutase (SOD1) is an important antioxidant gene, which catalyses the conversion of superoxide anion $O_2^{\bullet-}$ into other less toxic radical species to maintain low the ROS levels [51–53]. Downregulation of SOD1 expression correlated with increase in ROS levels [54]. In our results, we found that SOD1 decreased after Cu(II)NP treatment in both cell lines compared to Cu(I)NP treated group (A2780: 0.74 vs 0.85; SKOV-3: 0.70 vs 0.93; Fig. 5 **(f,h)**).

Since CuNP delivered even NO, it was quantified the expression level of inducible nitric oxide synthase gene (iNOS) known as NOS2, an NO regulated gene expression by a negative feedback loop [55]. As CuNP containing Cu^{+2} metals, in both cell lines NOS2 is significantly upregulated after treatment (Fig. 5 **(g,i)**), as Cu^{+2} induces NOS2 expression and as a consequence ROS [47,56], while there are no induction from their precursors (Fig. S8 **(b,d)**). SNP also inhibit cancer cell proliferation by the downregulation of c-myc gene expression through the inactivation of NF-κB [46].

As shown in Fig. 5 **(g,i),** the expression of NF-κB and c-myc was downregulated in SKOV-3 and only c-myc in A2780 cell lines compared to control. Instead, the cisPt treatment is reported to upregulate c-myc expression, in turn preventing apoptosis [57]. While, comparatively treatment with precursors (CuCl and $CuCl_2$) did not significantly alter the expression of NF-κB (Fig. S8 **(b,d)**).

3.7. CuNP have anticancer activity on human ovarian cancer organoids

Liver is the main organ for drug metabolism and excretion [58] to purify the blood from toxic compounds. Many studies reported the use of liver organoids to evaluate drug induced toxicity [59].

In our study, we further investigated CuNP cytotoxicity on normal mouse liver organoids to predict the in vivo biocompatibility. Immunohistochemistry was used to characterize organoids for premature (SOX9 and cytokeratin 19) and mature (HNF4α, albumin and E-cadherin) hepatocyte markers as previously published [60]. The IC_{50} values of Cu(I)NP (4.4 ± 0.8 μg/ml) are similar to CisPt (5.9 ± 1.5 μg/ml) (Fig. S9). Comparatively, Cu(II)NP (17.3 ± 0.7 μg/ml) were less toxic then Cu(I)NP and CisPt on mouse liver organoids but produced higher oxidative stress in tumour cells make them an ideal biocompatible therapeutic compound for cancer treatment.

Following, the CuNP were tested in ovarian cancer organoids, an uncurable disease. In late-stage ovarian cancer, 30% of patients develop ascites. Ascites are treated with chemotherapy and paracentesis is used to relieve the symptoms [61]. Ascites contains free floating cells, which develop intraperitoneal metastases [62]. To investigate the efficacy of CuNP, cancer organoids were generated from primary tumors and ascites. Cancer organoids provide an effective cancer model to evaluate the efficacy of therapeutic drugs [22,63,64], which could reproduce the clinical response of patients [65]. Organoids derived from high grade

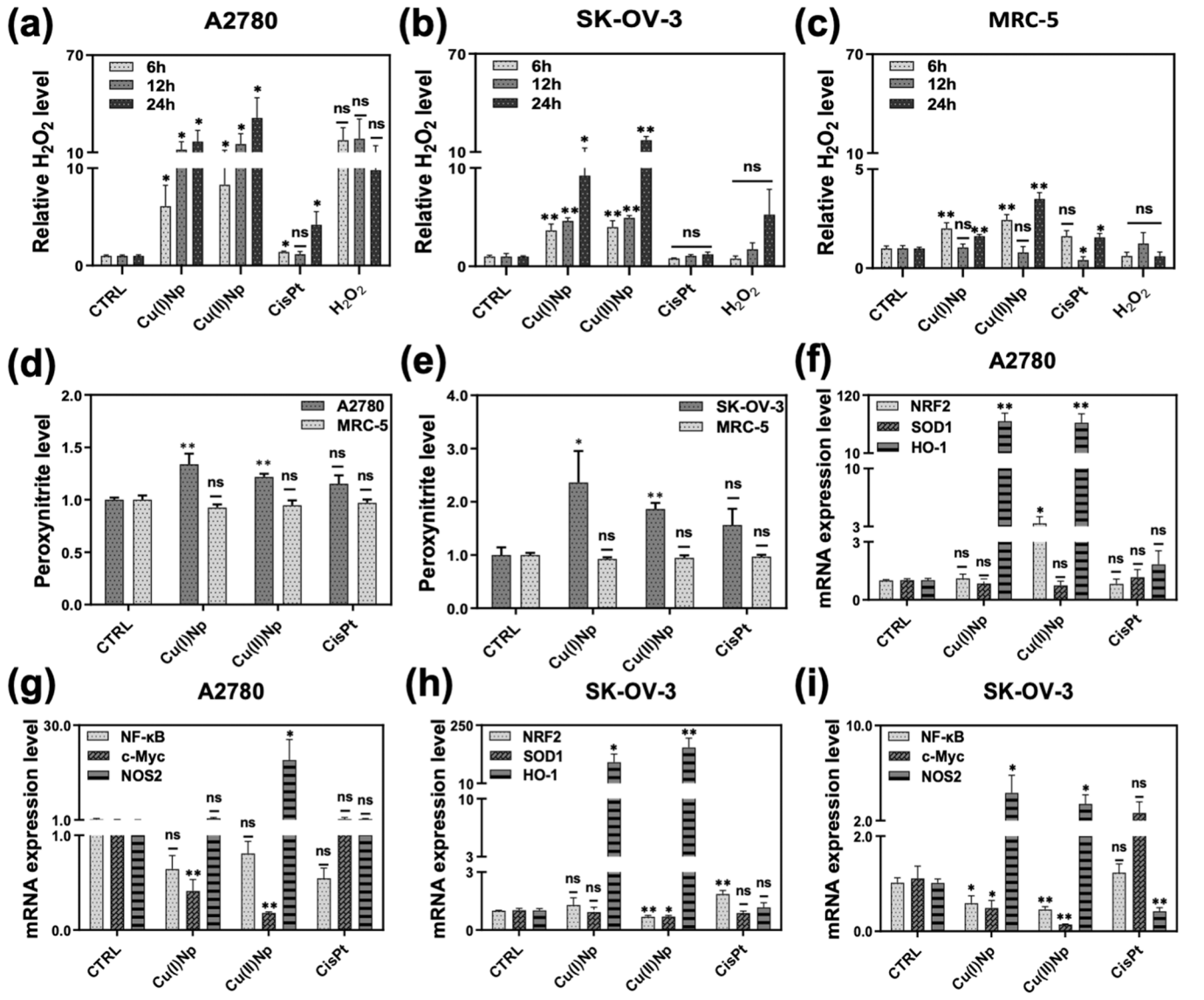

Fig. 5. CuNP generates multiple ROS in cancer cell lines. a-c, Relative H_2O_2 level measurement. **a,** A2780, **b,** SK-OV-3, **c,** MRC-5. **d-e,** Relative $ONOO^-$ level measurement. A2780, S-KO-V3, and MRC-5 **f-i,** qPCR analyses of selected genes. Bar graphs represent real-time RT-PCR analyses for mRNA expression of A2780 and SK-OV-3 cell lines after 24 h of CuNP treatment. **f, h,** NRF2, SOD1, HO-1, **g, i,** NF-κB, c-Myc, NOS2. Cells were incubated with CuNP (10 μg/ml), and CisPt (3 μg/ml; 10 μM) for 24 h; error bars indicate SEM. Data shown are two independent experiments of three replicates.

ovarian cancer primary tumors (Pat A, B) and two organoids derived from ascites (Pat C, D) **(**Table S4**)** were treated with CuNP. The IC_{50} values are effective in the range of 1.2 – 16.5 μg/ml **(**Fig. 6 **(a-d).**

In patient A and B, the in vitro sensibility to platinum and CuNP could be explained by the fact that PDTO were derived from treatment naïve tumor specimens. In Patient C and D, PDTO were harvest from cancer cells isolated from ascitic fluid that normally are resistant to chemotherapy. This explains the resistance against platinum **(**Fig. 6**(a-d)),** and Table S3**).** In accordance with the literature [66,67], immunohistochemistry analysis showed that ovarian organoids retained the characteristics of the original tumors as confirmed by the strong immunopositivity for CA-125 (cancer antigen 125), WT1 (Wilms' Tumor 1) and PAX8 (Paired box gene 8) that are markers of ovarian cancer **(**Fig. 6**e,** Fig. S10**).** Hence, our results highlight that ovarian cancer organoids preserve the molecular characteristics of the tissue of origin. The potency of CuNP on primary tumors and ascites suggests a possible therapeutic application of this novel material.

3.8. In vivo antitumor activity of CuNP

Since Cu(II)NP were less toxic on normal liver organoids and produce more ROS species than Cu(I)NP, the antitumor efficacy of Cu(II)NP was investigated using OVCAR-5 tumor bearing mice. When the tumor volume reached 50–100 mm^3, mice were treated intraperitoneally twice per week with 2 mg/kg of CisPt and 4 mg/kg of Cu(II)NP. After treatment, mice were examined every day for signs of toxicity (physical distresses). As shown in Fig. 6**f,** after Cu(II)NP treatment there is a reduction in tumor volume compared to control group, while no obvious body weight changes were observed **(**Fig. 6**g).** After being sacrificed, major organs (brain, heart, liver, lung, spleen, kidney, intestine and bone marrow) were collected. No apparent histopathological abnormalities were seen in Cu(II)NP treated group **(**Fig. S11**)**, representing a biocompatible therapeutic compound. Hence, these findings demonstrated the potential therapeutic application of the proposed novel material via multiple ROS generation.

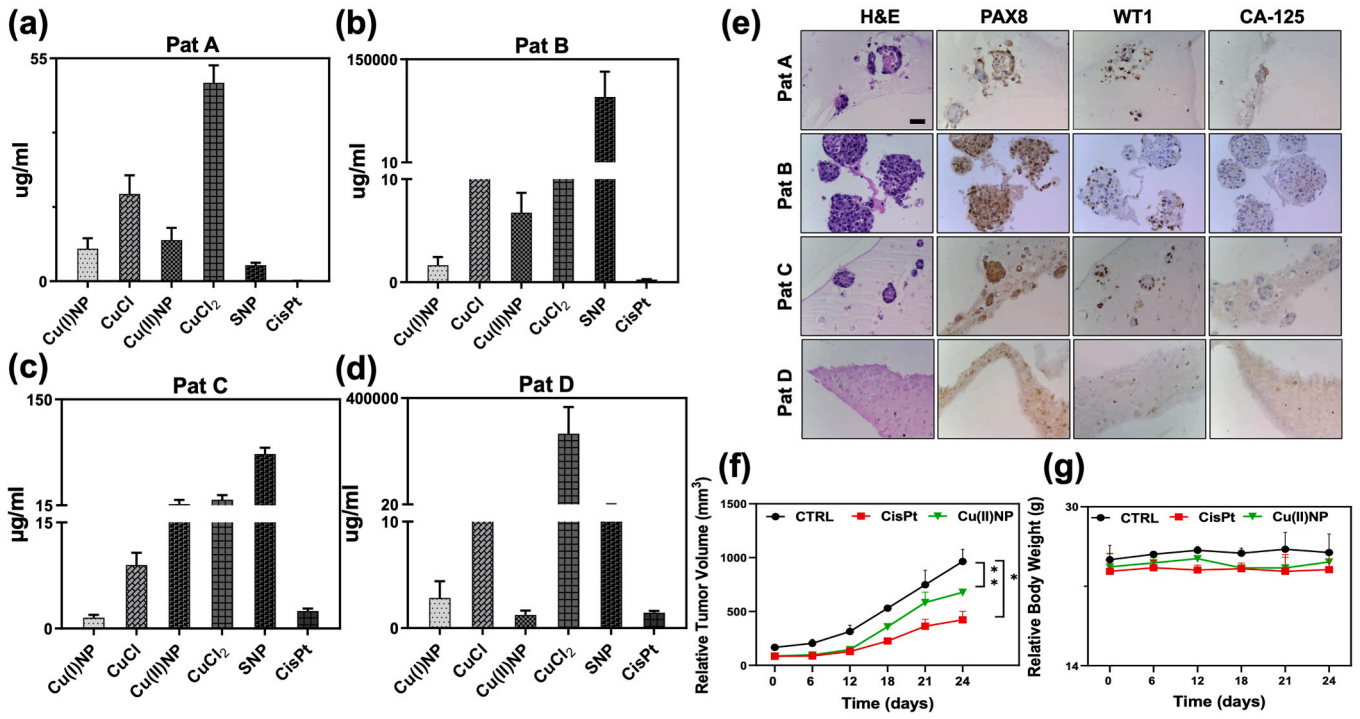

Fig. 6. Ex vivo anticancer activity of CuNP. (a-d) Cytotoxicity of CuNPs, and CisPt on cancer organoids derived from high grade tumor patients and from HGSOC ascite patients (Pat A-D) Error bars indicate SEM. **(e)** Hematoxylin & eosin staining and immunohistochemistry of (Pat A -D) organoids. CA-125, WT1 and PAX8 markers of HGSOC. 40x magnification; scale bar: 50 µm. **(f)** Relative tumor volume. Groups were considered statistically significant if $p < 0.05$ (*), $p < 0.01$ (**). Error bars indicate SEM. **(g)** body weight change of tumor-bearing mice after treatment with Cu(II)NP and cisPt.

4. Conclusions

In this manuscript, a self-therapeutic dual ROS generator nanosystem based on Fenton like reaction for cancer therapy was developed. Our results suggest that CuNP produced more ROS species in cancer cells due to acidic environment compared to normal cells. Additionally, NO reacts with $O_2^{-\bullet}$ to produce highly reactive $ONOO^-$ nitrogen specie as apoptotic inducer, thereby inducing more cancer cell destruction than healthy cells. Flow cytometry analysis showed a time dependent apoptosis compared to the precursors and CisPt. Moreover, internalization studies revealed that CuNP were involved in lysosomal membrane permeabilization through ROS production. The ROS production is higher in cancer cells than normal cells probably due to the acidic microenvironment, which contributes to the high selectivity. Additionally, these data are in line with the increase of cytochrome *c* release over time. Furthermore, the upregulation of oxidative stress genes confirmed that CuNP are more effective than the precursors and CisPt. Similarly, CuNP (Cu(I)NP, Cu(II)NP) showed a high therapeutic effect on ovarian cancer organoids independently of platinum resistance, while only Cu(II)NP showed lower toxicity on mouse liver organoids. In vivo study indicated that Cu(II)NP achieved significant therapeutic efficacy in tumor burden reduction with a self-generation of ROS species and an excellent biocompatibility. This innovative study offers a novel platform for the development of self-therapeutic multiple ROS producing materials, which is specific for the tumor microenvironment.

Funding

This research was funded by the Ministry of Health, Ricerca Corrente; Fondazione AIRC per la Ricerca sul Cancro (Grant AIRC IG23566).

CRediT authorship contribution statement

Asif Kanwal: Conceptualization, Investigation, Methodology, Writing – original draft, Writing – review & editing. **Adeel Muhammad:** Conceptualization, Investigation, Writing – original draft, Writing – review & editing. **Cemazar Maja:** Animal data analysis. **Rahman Md.:** Formal analysis. **Bartoletti Michele:** Clinical data analysis. **Canzonieri Vincenzo:** Funding acquisition and Pathological data analysis. **Rizzolio Flavio:** Funding acquisition, Supervision, Writing – review & editing. **Caligiuri Isabella:** Supervision. **Kranjc Brezar Simona:** Animal data analysis.

Declaration of Competing Interest

The authors declare that they have no known competing financial interests or personal relationships that could have appeared to influence the work reported in this paper.

Data availability

Data will be made available after a reasonable request.

Appendix A. Supporting information

Supplementary data associated with this article can be found in the online version at doi:10.1016/j.biopha.2023.116017.

References

[1] H. Deng, Z. Yang, X. Pang, C. Zhao, J. Tian, Z. Wang, X. Chen, Self-sufficient copper peroxide loaded pKa-tunable nanoparticles for lysosome-mediated chemodynamic therapy, Nano Today 42 (2022) 101337, https://doi.org/10.1016/J.NANTOD.2021.101337.

[2] L.-S. Lin, T. Huang, J. Song, X.-Y. Ou, Z. Wang, H. Deng, R. Tian, Y. Liu, J.-F. Wang, Y. Liu, G. Yu, Z. Zhou, S. Wang, G. Niu, H.-H. Yang, X. Chen, Synthesis of Copper Peroxide Nanodots for H 2 O 2 Self-Supplying Chemodynamic Therapy, (2019). https://doi.org/10.1021/jacs.9b03457.

[3] J.X. Fan, M.Y. Peng, H. Wang, H.R. Zheng, Z.L. Liu, C.X. Li, X.N. Wang, X.H. Liu, S. X. Cheng, X.Z. Zhang, Engineered bacterial bioreactor for tumor therapy via

fenton-like reaction with localized H 2 O 2 generation, Adv. Mater. 31 (2019), https://doi.org/10.1002/ADMA.201808278.
[4] H. Ranji-Burachaloo, P.A. Gurr, D.E. Dunstan, G.G. Qiao, Cancer treatment through nanoparticle-facilitated fenton reaction, ACS Nano 12 (2018) 11819–11837, https://doi.org/10.1021/ACSNANO.8B07635.
[5] L. Zhang, S.S. Wan, C.X. Li, L. Xu, H. Cheng, X.Z. Zhang, An adenosine triphosphate-responsive autocatalytic fenton nanoparticle for tumor ablation with self-supplied H 2 O 2 and acceleration of Fe(III)/Fe(II) conversion, Nano Lett. 18 (2018) 7609–7618, https://doi.org/10.1021/ACS.NANOLETT.8B03178.
[6] Z. Tang, Y. Liu, M. He, W. Bu, Chemodynamic therapy: tumour microenvironment-mediated fenton and fenton-like reactions, Angew. Chem. 131 (2019) 958–968, https://doi.org/10.1002/ANGE.201805664.
[7] P. Zhao, Z. Tang, X. Chen, Z. He, X. He, M. Zhang, Y. Liu, D. Ren, K. Zhao, W. Bu, Ferrous-cysteine–phosphotungstate nanoagent with neutral pH fenton reaction activity for enhanced cancer chemodynamic therapy, Mater. Horiz. 6 (2019) 369–374, https://doi.org/10.1039/C8MH01176A.
[8] Y. Li, R. Jia, H. Lin, X. Sun, F. Qu, Y. Li, H. Lin, F. Qu, R. Jia, X.L. Sun, Synthesis of MoSe2/CoSe2 nanosheets for NIR-enhanced chemodynamic therapy via synergistic in-situ H2O2 production and activation, Adv. Funct. Mater. 31 (2021) 2008420, https://doi.org/10.1002/ADFM.202008420.
[9] Y. Liu, X. Ji, W.W.L. Tong, D. Askhatova, T. Yang, H. Cheng, Y. Wang, J. Shi, Engineering multifunctional RNAi nanomedicine to concurrently target cancer hallmarks for combinatorial therapy, Angew. Chem. 130 (2018) 1526–1529, https://doi.org/10.1002/ANGE.201710144.
[10] S. Wang, Z. Wang, G. Yu, Z. Zhou, O. Jacobson, Y. Liu, Y. Ma, F. Zhang, Z.-Y. Chen, X. Chen, S. Wang, Z.-Y. Chen, Z. Wang, G. Yu, Z. Zhou, O. Jacobson, Y. Liu, Y. Ma, F. Zhang, X. Chen, Tumor-specific drug release and reactive oxygen species generation for cancer chemo/chemodynamic combination therapy, Adv. Sci. 6 (2019) 1801986, https://doi.org/10.1002/ADVS.201801986.
[11] M. Huo, L. Wang, Y. Chen, J. Shi, Tumor-selective catalytic nanomedicine by nanocatalyst delivery, 2017 8:1, Nat. Commun. 8 (2017) 1–12, https://doi.org/10.1038/s41467-017-00424-8.
[12] W.P. Li, C.H. Su, Y.C. Chang, Y.J. Lin, C.S. Yeh, Ultrasound-induced reactive oxygen species mediated therapy and imaging using a fenton reaction activable polymersome, ACS Nano 10 (2016) 2017–2027, https://doi.org/10.1021/ACSNANO.5B06175/SUPPL_FILE/NN5B06175_SI_001.PDF.
[13] S. Fu, R. Yang, L. Zhang, W. Liu, G. Du, Y. Cao, Z. Xu, H. Cui, Y. Kang, P. Xue, Biomimetic CoO@AuPt nanozyme responsive to multiple tumor microenvironmental clues for augmenting chemodynamic therapy, Biomaterials 257 (2020) 120279, https://doi.org/10.1016/J.BIOMATERIALS.2020.120279.
[14] S. Gao, H. Lin, H. Zhang, H. Yao, Y. Chen, J. Shi, S. Gao, H. Lin, H. Yao, Y. Chen, J. Shi, H. Zhang, Nanocatalytic tumor therapy by biomimetic dual inorganic nanozyme-catalyzed cascade reaction, Adv. Sci. 6 (2019) 1801733, https://doi.org/10.1002/ADVS.201801733.
[15] C.C. Huang, W.T. Chia, M.F. Chung, K.J. Lin, C.W. Hsiao, C. Jin, W.H. Lim, C. C. Chen, H.W. Sung, An implantable depot that can generate oxygen in situ for overcoming hypoxia-induced resistance to anticancer drugs in chemotherapy, J. Am. Chem. Soc. 138 (2016) 5222–5225, https://doi.org/10.1021/JACS.6B01784/SUPPL_FILE/JA6B01784_SI_001.PDF.
[16] S. Heigold, C. Sers, W. Bechtel, B. Ivanovas, R. Schäfer, G. Bauer, Nitric oxide mediates apoptosis induction selectively in transformed fibroblasts compared to nontransformed fibroblasts, Carcinogenesis 23 (2002) 929–941, https://doi.org/10.1093/CARCIN/23.6.929.
[17] Y. Chen, Z.H. Li, P. Pan, R.Y. Zeng, X.Z. Zhang, Tumor-specific ONOO- nanogenerator for improved drug delivery and enhanced chemotherapy of tumor, ACS Nano 15 (2021) 11514–11525, https://doi.org/10.1021/ACSNANO.1C01312/SUPPL_FILE/NN1C01312_SI_001.PDF.
[18] C. Szabó, H. Ischiropoulos, R. Radi, Peroxynitrite: biochemistry, pathophysiology and development of therapeutics, 2007 6:8, Nat. Rev. Drug Discov. 6 (2007) 662–680, https://doi.org/10.1038/nrd2222.
[19] Z. Du, X. Zhang, Z. Guo, J. Xie, X. Dong, S. Zhu, J. Du, Z. Gu, Y. Zhao, Z. Du, X. Zhang, Z. Guo, J. Xie, X. Dong, S. Zhu, Z. Gu, Y. Zhao, J. Du, X-ray-controlled generation of peroxynitrite based on nanosized LiLuF4:Ce3+ scintillators and their applications for radiosensitization, Adv. Mater. 30 (2018) 1804046, https://doi.org/10.1002/ADMA.201804046.
[20] D. Jiang, T. Yue, G. Wang, C. Wang, H. Cao, Y. Gao, C. Chen, Peroxynitrite (ONOO−) generation from the HA-TPP@NORM nanoparticles based on synergistic interactions between nitric oxide and photodynamic therapies for elevating anticancer efficiency, N. J. Chem. 44 (2019) 162–170, https://doi.org/10.1039/C9NJ04763H.
[21] M. Adeel, F. Duzagac, V. Canzonieri, F. Rizzolio, Self-therapeutic nanomaterials for cancer therapy: a review, ACS Appl. Nano Mater. 3 (2020) 4962–4971, https://doi.org/10.1021/ACSANM.0C00762.
[22] M. Adeel, S. Parisi, M. Mauceri, K. Asif, M. Bartoletti, F. Puglisi, I. Caligiuri, M. M. Rahman, V. Canzonieri, F. Rizzolio, Self-therapeutic cobalt hydroxide nanosheets (Co(OH)2NS) for ovarian cancer therapy, ACS Omega 6 (2021) 28611–28619, https://doi.org/10.1021/ACSOMEGA.1C03010/SUPPL_FILE/AO1C03010_SI_001.PDF.
[23] K. Asif, M. Adeel, M.M. Rahman, A.A. Sfriso, M. Bartoletti, V. Canzonieri, F. Rizzolio, I. Caligiuri, Silver nitroprusside as an efficient chemodynamic therapeutic agent and a peroxynitrite nanogenerator for targeted cancer therapies, J. Adv. Res (2023), https://doi.org/10.1016/J.JARE.2023.03.005.
[24] K. Asif, M. Adeel, M.M. Rahman, I. Caligiuri, T. Perin, M. Cemazar, V. Canzonieri, F. Rizzolio, Iron nitroprusside as a chemodynamic agent and inducer of ferroptosis for ovarian cancer therapy, J. Mater. Chem. B 11 (2023) 3124–3135, https://doi.org/10.1039/D2TB02691K.
[25] L. Reguera, Y. Avila, E. Reguera, Transition metal nitroprussides: crystal and electronic structure, and related properties, Coord. Chem. Rev. 434 (2021) 213764, https://doi.org/10.1016/J.CCR.2020.213764.
[26] J. Rodríguez-Hernández, L. Reguera, A.A. Lemus-Santana, E. Reguera, Silver nitroprusside: atypical coordination within the metal nitroprussides series, Inorg. Chim. Acta 428 (2015) 51–56, https://doi.org/10.1016/J.ICA.2014.12.023.
[27] A. Djebli, A. Boudjemaa, H. Bendjeffal, H. Mamine, T. Metidji, H. Bekakria, Y. Bouhedja, Photocatalytic degradation of methyl orange using Zn@[Fe(CN)5NO] complex under sunlight irradiation, Https://Doi.Org/10.1080/24701556.2020.1735428. 50 (2020) 1115–1122. https://doi.org/10.1080/24701556.2020.1735428.
[28] C. Romao, M.M. Barsan, I.S. Butler, D.F.R. Gilson, A high-pressure micro-Raman spectroscopic study of copper cyanide, CuCN, J. Mater. Sci. 45 (2010) 2518–2520, https://doi.org/10.1007/S10853-010-4232-Y/TABLES/1.
[29] M.M. Rahman, E. Klugmann-Radziemska, Low-cost and efficient nickel nitroprusside/graphene nanohybrid electrocatalysts as counter electrodes for dye-sensitized solar cells, 2021, Vol. 14, Page 6563, Materials 14 (2021) 6563, https://doi.org/10.3390/MA14216563.
[30] H. Razmi, H. Heidari, Nafion/lead nitroprusside nanoparticles modified carbon ceramic electrode as a novel amperometric sensor for L-cysteine, Anal. Biochem 388 (2009) 15–22, https://doi.org/10.1016/J.AB.2009.01.036.
[31] A. Mullaliu, G. Aquilanti, J.R. Plaisier, M. Giorgetti, B. Barbiellini, J. Kuriplach, R. Saniz, Cross-investigation on copper nitroprusside: combining XRD and XAS for in-depth structural insights, 2021, Vol. 6, Page 27, Condens. Matter 6 (2021) 27, https://doi.org/10.3390/CONDMAT6030027.
[32] A. Cano, J. Rodríguez-Hernández, A. Shchukarev, E. Reguera, Intercalation of pyrazine in layered copper nitroprusside: synthesis, crystal structure and XPS study, J. Solid State Chem. 273 (2019) 1–10, https://doi.org/10.1016/J.JSSC.2019.02.015.
[33] K.T. Lee, Y.J. Lu, S.C. Chiu, W.C. Chang, E.Y. Chuang, S.Y. Lu, Heterogeneous fenton reaction enabled selective colon cancerous cell treatment, 2018 8:1, Sci. Rep. 8 (2018) 1–10, https://doi.org/10.1038/s41598-018-34499-0.
[34] Q. An, C. Sun, D. Li, K. Xu, J. Guo, C. Wang, Peroxidase-like activity of Fe3O4@ carbon nanoparticles enhances ascorbic acid-induced oxidative stress and selective damage to PC-3 prostate cancer cells, ACS Appl. Mater. Interfaces 5 (2013) 13248–13257, https://doi.org/10.1021/AM4042367/SUPPL_FILE/AM4042367_SI_001.PDF.
[35] H. Ranji-Burachaloo, F. Karimi, K. Xie, Q. Fu, P.A. Gurr, D.E. Dunstan, G.G. Qiao, MOF-mediated destruction of cancer using the cell's own hydrogen peroxide, ACS Appl. Mater. Interfaces 9 (2017) 33599–33608, https://doi.org/10.1021/ACSAMI.7B07981/SUPPL_FILE/AM7B07981_SI_001.PDF.
[36] C. Zhang, W. Bu, D. Ni, S. Zhang, Q. Li, Z. Yao, J. Zhang, H. Yao, Z. Wang, J. Shi, Synthesis of iron nanometallic glasses and their application in cancer therapy by a localized fenton reaction, Angew. Chem. 128 (2016) 2141–2146, https://doi.org/10.1002/ANGE.201510031.
[37] J. Fu, Y. Shao, L. Wang, Y. Zhu, Lysosome-controlled efficient ROS overproduction against cancer cells with a high pH-responsive catalytic nanosystem, Nanoscale 7 (2015) 7275–7283, https://doi.org/10.1039/C5NR00706B.
[38] S. Desagher, J.C. Martinou, Mitochondria as the central control point of apoptosis, Trends Cell Biol. 10 (2000) 369–377, https://doi.org/10.1016/S0962-8924(00)01803-1.
[39] J. Pourahmad, S. Ross, P.J. O'Brien, Lysosomal involvement in hepatocyte cytotoxicity induced by Cu(2+) but not Cd(2+), Free Radic. Biol. Med 30 (2001) 89–97, https://doi.org/10.1016/S0891-5849(00)00450-0.
[40] V. Aliko, G. Hajdaraj, A. Caci, C. Faggio, Copper induced lysosomal membrane destabilisation in haemolymph cells of mediterranean green crab (**Carcinus aestuarii**, Nardo, 1847) from the Narta Lagoon (Albania), Braz. Arch. Biol. Technol. 58 (2015) 750–756, https://doi.org/10.1590/S1516-89132015050244.
[41] P. Boya, G. Kroemer, Lysosomal membrane permeabilization in cell death, Oncogene 27 (2008) 6434–6451, https://doi.org/10.1038/onc.2008.310.
[42] J.R. Hornick, S. Vangveravong, D. Spitzer, C. Abate, F. Berardi, P. Goedegebuure, R.H. MacH, W.G. Hawkins, Lysosomal membrane permeabilization is an early event in sigma-2 receptor ligand mediated cell death in pancreatic cancer, J. Exp. Clin. Cancer Res. 31 (2012) 1–11, https://doi.org/10.1186/1756-9966-31-41.
[43] A.C. Johansson, H. Appelqvist, C. Nilsson, K. Kågedal, K. Roberg, K. Öllinger, Regulation of apoptosis-associated lysosomal membrane permeabilization, Apoptosis 15 (2010) 527–540, https://doi.org/10.1007/s10495-009-0452-5.
[44] Z. Luo, Q. Zhao, J. Liu, J. Liao, R. Peng, Y. Xi, Z. Diwu, Fluorescent real-time quantitative measurements of intracellular peroxynitrite generation and inhibition, Anal. Biochem 520 (2017) 44–48, https://doi.org/10.1016/J.AB.2017.01.001.
[45] M.N.K. Sumitani, R. Kamijo, Cytotoxic effect of sodium nitroprusside on cancer cells: involvement of apoptosis and suppression of c-myc and c-myb proto-oncogene expression - PubMed, Anticancer Res (1997) 865–871, https://pubmed.ncbi.nlm.nih.gov/9137419/ (accessed January 1, 2022).
[46] S.W. Park, L.N. Wei, Regulation of c-myc gene by nitric oxide via inactivating NF-κB complex in P19 mouse embryonal carcinoma cells *, J. Biol. Chem. 278 (2003) 29776–29782, https://doi.org/10.1074/JBC.M303306200.
[47] M. Majewski, B. Lis, B. Olas, K. Ognik, J. Juśkiewicz, Dietary supplementation with copper nanoparticles influences the markers of oxidative stress and modulates vasodilation of thoracic arteries in young Wistar rats, PLoS One 15 (2020), https://doi.org/10.1371/JOURNAL.PONE.0229282.
[48] C. Song, H. Heping, Y. Shen, S. Jin, D. Li, A. Zhang, X. Ren, K. Wang, L. Zhang, J. Wang, D. Shi, AMPK/p38/Nrf2 activation as a protective feedback to restrain oxidative stress and inflammation in microglia stimulated with sodium fluoride, Chemosphere 244 (2020), https://doi.org/10.1016/J.CHEMOSPHERE.2019.125495.

[49] L. Xiong, J. Xie, C. Song, J. Liu, J. Zheng, C. Liu, X. Zhang, P. Li, F. Wang, The activation of Nrf2 and its downstream regulated genes mediates the antioxidative activities of xueshuan xinmaining tablet in human umbilical vein endothelial cells, Evid. Based Complement Altern. Med 2015 (2015) 187265, https://doi.org/10.1155/2015/187265.
[50] L. Zou, G. Cheng, C. Xu, H. Liu, Y. Wang, N. Li, X. Fan, C. Zhu, W. Xia, Copper Nanoparticles Induce Oxidative Stress via the Heme Oxygenase 1 Signaling Pathway in vitro Studies , Int J Nanomedicine. 16 (2021) 1565–1573. https://doi.org/10.2147/IJN.S292319.
[51] I. Fridovich, SUPEROXIDE RADICAL AND SUPEROXIDE DISMUTASES, 64 (1995) 97–112.
[52] Y. Sheng, I.A. Abreu, D.E. Cabelli, M.J. Maroney, A.F. Miller, M. Teixeira, J. S. Valentine, Superoxide dismutases and superoxide reductases, Chem. Rev. 114 (2014) 3854–3918, https://doi.org/10.1021/CR4005296.
[53] X. Li, Y. Chen, J. Zhao, J. Shi, M. Wang, S. Qiu, Y. Hu, Y. Xu, Y. Cui, C. Liu, C. Liu, The specific inhibition of SOD1 selectively promotes apoptosis of cancer cells via regulation of the ROS signaling network, Oxid. Med Cell Longev. 2019 (2019), https://doi.org/10.1155/2019/9706792.
[54] Z.F. Lin, H.B. Xu, J.Y. Wang, Q. Lin, Z. Ruan, F.B. Liu, W. Jin, H.H. Huang, X. Chen, SIRT5 desuccinylates and activates SOD1 to eliminate ROS, Biochem Biophys. Res Commun. 441 (2013) 191–195, https://doi.org/10.1016/J.BBRC.2013.10.033.
[55] Z. yuan Xia, X. yuan Wang, X. Chen, Z. Xia, Effect of NO donor sodium nitroprusside on lipopolysaccharide induced acute lung injury in rats, Injury 38 (2007) 53–59, https://doi.org/10.1016/J.INJURY.2006.09.021.
[56] S. Cuzzocrea, T. Persichini, L. Dugo, M. Colasanti, G. Musci, Copper induces type II nitric oxide synthase in vivo, Free Radic. Biol. Med 34 (2003) 1253–1262, https://doi.org/10.1016/S0891-5849(03)00110-2.
[57] L. Cui, B. Liang, Y. Yang, M. Zhu, J. Kwong, H. Zheng, C.C. Wang, Inhibition of coiled coil domain containing protein 69 enhances platinum-induced apoptosis in ovarian cancer cells, Oncotarget 8 (2017) 101634–101648, https://doi.org/10.18632/ONCOTARGET.21356.
[58] A. Brooks, X. Liang, Y. Zhang, C.X. Zhao, M.S. Roberts, H. Wang, L. Zhang, D.H. G. Crawford, Liver organoid as a 3D in vitro model for drug validation and toxicity assessment, Pharm. Res 169 (2021) 105608, https://doi.org/10.1016/j.phrs.2021.105608.
[59] S. Palazzolo, M. Hadla, C.R. Spena, I. Caligiuri, R. Rotondo, M. Adeel, V. Kumar, G. Corona, V. Canzonieri, G. Toffoli, F. Rizzolio, An effective multi-stage liposomal DNA origami nanosystem for in vivo cancer therapy, 2019, Vol. 11, Page 1997, Cancers 11 (2019) 1997, https://doi.org/10.3390/CANCERS11121997.
[60] S. Palazzolo, M. Hadla, C.R. Spena, I. Caligiuri, R. Rotondo, M. Adeel, V. Kumar, G. Corona, V. Canzonieri, G. Toffoli, F. Rizzolio, An effective multi-stage liposomal DNA origami nanosystem for in vivo cancer therapy, 2019, Vol. 11, Page 1997, Cancers 11 (2019) 1997, https://doi.org/10.3390/CANCERS11121997.
[61] E. Kipps, D.S.P. Tan, S.B. Kaye, Meeting the challenge of ascites in ovarian cancer: new avenues for therapy and research, 2013 13:4, Nat. Rev. Cancer 13 (2013) 273–282, https://doi.org/10.1038/nrc3432.
[62] E. Smolle, V. Taucher, J.H.-A. research, undefined 2014, Malignant ascites in ovarian cancer and the role of targeted therapeutics, Ar.Iiarjournals.Org. 34 (2014) 1553–1561.
[63] T. Scattolin, I. Pessotto, E. Cavarzerani, V. Canzonieri, L. Orian, N. Demitri, C. Schmidt, A. Casini, E. Bortolamiol, F. Visentin, F. Rizzolio, S.P. Nolan, Indenyl and allyl palladate complexes bearing N-heterocyclic carbene ligands: an easily accessible class of new anticancer drug candidates, Eur. J. Inorg. Chem. 2022 (2022) e202200103, https://doi.org/10.1002/ejic.202200103.
[64] T. Scattolin, E. Bortolamiol, F. Visentin, S. Palazzolo, I. Caligiuri, T. Perin, V. Canzonieri, N. Demitri, F. Rizzolio, A. Togni, Palladium(II)-η3-Allyl complexes bearing N-trifluoromethyl n-heterocyclic carbenes: a new generation of anticancer agents that restrain the growth of high-grade serous ovarian cancer tumoroids, Chem. - A Eur. J. 26 (2020) 11868–11876, https://doi.org/10.1002/chem.202002199.
[65] S.J. Hill, B. Decker, E.A. Roberts, N.S. Horowitz, M.G. Muto, M.J. Worley, C. M. Feltmate, M.R. Nucci, E.M. Swisher, H. Nguyen, C. Yang, R. Morizane, B. S. Kochupurakkal, K.T. Do, P.A. Konstantinopoulos, J.F. Liu, J.V. Bonventre, U. A. Matulonis, G.I. Shapiro, R.S. Berkowitz, C.P. Crum, A.D. D'Andrea, Prediction of DNA repair inhibitor response in short-term patient-derived ovarian cancer organoids, Cancer Discov. 8 (2018) 1404–1421, https://doi.org/10.1158/2159-8290.CD-18-0474.
[66] C. Tornos, R. Soslow, S. Chen, M. Akram, A.J. Hummer, N. Abu-Rustum, L. Norton, L.K. Tan, Expression of WT1, CA 125, and GCDFP-15 as useful markers in the differential diagnosis of primary ovarian carcinomas versus metastatic breast cancer to the ovary, Am. J. Surg. Pathol. 29 (2005) 1482–1489, https://doi.org/10.1097/01.PAS.0000176429.88702.36.
[67] L. Liliac, M. Luisa Carcangiu, S. Canevari, I.D. Căruntu, D.G.C. Apostol, M. Danciu, M. Onofriescu, C. Amălinei, The value of PAX8 and WT1 molecules in ovarian cancer diagnosis, Rom. J. Morphol. Embryol. 54 (2013) 17–27.